



Controllable synthesis of $\text{Co}_{1-x}\text{M}_x\text{Fe}_2\text{O}_4$ nanoparticles (M = Zn, Cu, and Mn; $x = 0.0$ and 0.5) by cost-effective sol–gel approach: analysis of structure, elastic, thermal, and magnetic properties

M. I. A. Abdel Maksoud¹ · Gharieb S. El-Sayyad^{2,3} · M. Abd Elkodous^{4,5} · A. S. Awed⁶

Received: 30 January 2020 / Revised: 20 April 2020 / Accepted: 28 April 2020 / Published online: 9 May 2020
© Springer Science+Business Media, LLC, part of Springer Nature 2020

Abstract

Substitutions of cations were considered to be the main way for improving the performance of ferrite nanocrystalline structures. In this paper, non-magnetic and magnetic ions were conducted to substitute cobalt spinel ferrite nanoparticles CoFe_2O_4 NPs (CFO NPs). The studied $\text{Co}_{1-x}\text{M}_x\text{Fe}_2\text{O}_4$; M = Zn, Cu, and Mn; $x = 0.00$, and 0.50) samples were synthesized through a cost-effective sol–gel technique. The outstanding properties of the samples are addressed using XRD, FTIR, the inductively coupled plasma optical emission spectrometer (ICP-OES), Raman analyses, HR-TEM, BET surface area analyzer, the energy-dispersive X-ray analysis spectra (EDX), and vibrating sample magnetometer (VSM). The Rietveld analysis and FTIR spectroscopic measurements revealed the successful synthesis of the cubic spinel phase. HR-TEM images reveal that the particles of all samples had spherical shape in the nanometer range. Moreover, the synthesized ZCFO NPs has the highest specific surface area of $26.87 \text{ m}^2/\text{g}$ than other samples. Interestingly, the determined Debye temperature from both elastic and infrared data was in a good conformity with each other. Finally, the values of saturation magnetization (M_s) increased from 39.128 emu/g for CCFO NPs to 68.419 emu/g for CFO NPs. The observed coercive field increased from 213.93 G for ZCFO NPs sample to 1914.85 G for CCFO NPs.

1 Introduction

Nanocrystalline spinel ferrites have many interesting structural [1], elastic [2], magnetic [3], thermal [4], electrical [5], optical [6], and dielectric properties [7]. These attractive properties make them promising materials for many

applications such as high-performance super-capacitors [8–10], microwave absorber [11], biosensors [12], photocatalysts [13], wastewater remediation [14], antennas [15], transformers cores [16], and in hyperthermia uses [17].

The application of spinel ferrites depends on many parameters such as the preparation route and metals' substitution at the preferred sub-lattices [18, 19]. The re-distribution of cations at the tetrahedral site (A-site) and the octahedral site (B-site) by substituting any metal ions in the

Electronic supplementary material The online version of this article (<https://doi.org/10.1007/s10854-020-03518-0>) contains supplementary material, which is available to authorized users.

✉ M. I. A. Abdel Maksoud
muhamadmqsod@gmail.com; muhamad.mqsod@eaea.org.eg

✉ Gharieb S. El-Sayyad
adham_adham699@yahoo.com;
Gharieb.Elsayyad@eaea.org.eg

¹ Materials Science Lab., Radiation Physics Department, National Center for Radiation Research and Technology (NCRRT), Atomic Energy Authority, Cairo, Egypt

² Chemical Engineering Department, Military Technical College (MTC), Egyptian Armed Forces, Cairo, Egypt

³ Drug Radiation Research Department, National Center for Radiation Research and Technology (NCRRT) Atomic Energy Authority, Cairo, Egypt

⁴ Department of Electrical and Electronic Information Engineering, Toyohashi University of Technology, Toyohashi, Aichi 441-8580, Japan

⁵ Center for Nanotechnology (CNT), School of Engineering and Applied Sciences, Nile University, Sheikh Zayed, Giza 16453, Egypt

⁶ Higher Institute of Engineering and Technology, Manzala, Egypt

system of nanocrystalline ferrite, has an extremely critical impact on managing the properties of this system [20].

Therefore, the replacement with metal ions such as Ni, Cu, Zn, and/or Mn enhances and controls the properties of spinel ferrites [6, 21]. Recently, various methods of synthesis are paving the way to fabricate materials with desired magnetic properties suited for specific applications [22–28]. The sol–gel method represents the more effective and practical route to promote the purity and homogeneity of the fabricated ferrite NPs. The sol–gel technique is a unique low-temperature procedure which includes hydrolysis and intensification reactions of the metals salts to produce the required inorganic network [29].

Among spinel ferrites, nanocrystalline cobalt ferrite nanoparticles (CFO NPs) possess unique physical properties such as relatively higher coercivity and moderate magnetization saturation allowing them for applications in distinct technologies [17, 30–36]. Like other spinel ferrites, CFO NPs are strongly affected by replacing metal cations. Recently, the effect of replacing Co^{2+} ions by Zn^{2+} ions on the characteristics of CFO NPs has been studied [37].

XRD and FTIR data clearly revealed the cubic spinel phase of $\text{Co}_{1-x}\text{Zn}_x\text{Fe}_2\text{O}_4$ NPs with two absorption bands ν_1 and ν_2 , which are attributed to the stretching of metal ions in the tetrahedral and octahedral sites, respectively. In addition, hardness parameters of the compounds were changed with grain size variation. Moreover, M_S value has a direct relation with the particle size, also the coercivity in the range of (430.4–73.56) Oe.

The elastic parameters and θ_D of ferrite NPs were reduced after substitution for CFO NPs. In another context, the synthesis and different properties of copper substituted Co–Ni ferrite ($\text{Co}_{0.5}\text{Ni}_{0.5-x}\text{Cu}_x\text{Fe}_2\text{O}_4$) have been also reported [38]. The results showed that the experimental and theoretical densities (d_x) and (d_b) were significantly changed by increasing the concentration of Cu^{2+} ions. Moreover, the values of M_S were in the range of (40–60) emu/g, while the H_C values were in the range of (191–885) Oe. The resistivity of the samples was enhanced by substitution of Ni ions by Cu ions. Furthermore, CFO NPs were synthesized using sol–gel auto-combustion technique and substituted with transition metals (i.e., $\text{CoM}_x\text{Fe}_{2-x}\text{O}_4$; $M = \text{Cr, Zn, Cu, and Ni}$) for heterogeneous catalysis [39]. The results indicated that the catalytic activity of the samples was increased by increasing metal content.

In this paper, we are presenting a comparative study for the effect of replacing Co^{2+} ions by non-magnetic ions (Zn^{2+}) and magnetic ions like Cu^{2+} and Mn^{2+} ions on the properties of cobalt ferrites CFO NPs ($\text{Co}_{1-x}\text{M}_x\text{Fe}_2\text{O}_4$; $M = \text{Zn, Cu and Mn}$; $x = 0.00, \text{ and } 0.50$), which were prepared by a cost-effective sol–gel method. We offer an original research paper within the theme of nanostructured magnetic materials and with fully identified and frequently

characterized in more detailed validation such as XRD, FTIR, ICP-OES, Raman, HR-TEM, BET, EDX, SEM/EDX mapping, and VSM to establish a prominent and complete description of the synthesized materials.

Briefly, for the first time, focusing the attention on the magnetic is based on spinel $\text{Co}_{1-x}\text{M}_x\text{Fe}_2\text{O}_4$ NPs ($M = \text{Zn, Cu and Mn}$; $x = 0.00, \text{ and } 0.50$). According to Hund's rule, the atomic magnetic moment of Co^{2+} , Zn^{2+} , Cu^{2+} , and Mn^{2+} is ($3 \mu_B$), ($0 \mu_B$), ($1 \mu_B$), and ($4.5 \mu_B$), respectively. Due to the variant atomic magnetic moment and ionic radii of the substituted metal ions, we expect that the structural, elastic, and magnetic properties of CFO NPs will be strongly influenced. Furthermore, the elastic constants of ferrite NPs have been determined.

Finally, the effect of metals' substitution on the magnetic properties of the synthesized ferrite NPs was extensively studied. The tested samples CoFe_2O_4 , $\text{Zn}_{0.5}\text{Co}_{0.5}\text{Fe}_2\text{O}_4$, $\text{Cu}_{0.5}\text{Co}_{0.5}\text{Fe}_2\text{O}_4$, and $\text{Mn}_{0.5}\text{Co}_{0.5}\text{Fe}_2\text{O}_4$ NPs were symbolized as CFO, ZCFO, CCFO, and MCFO, respectively.

2 Materials and methods

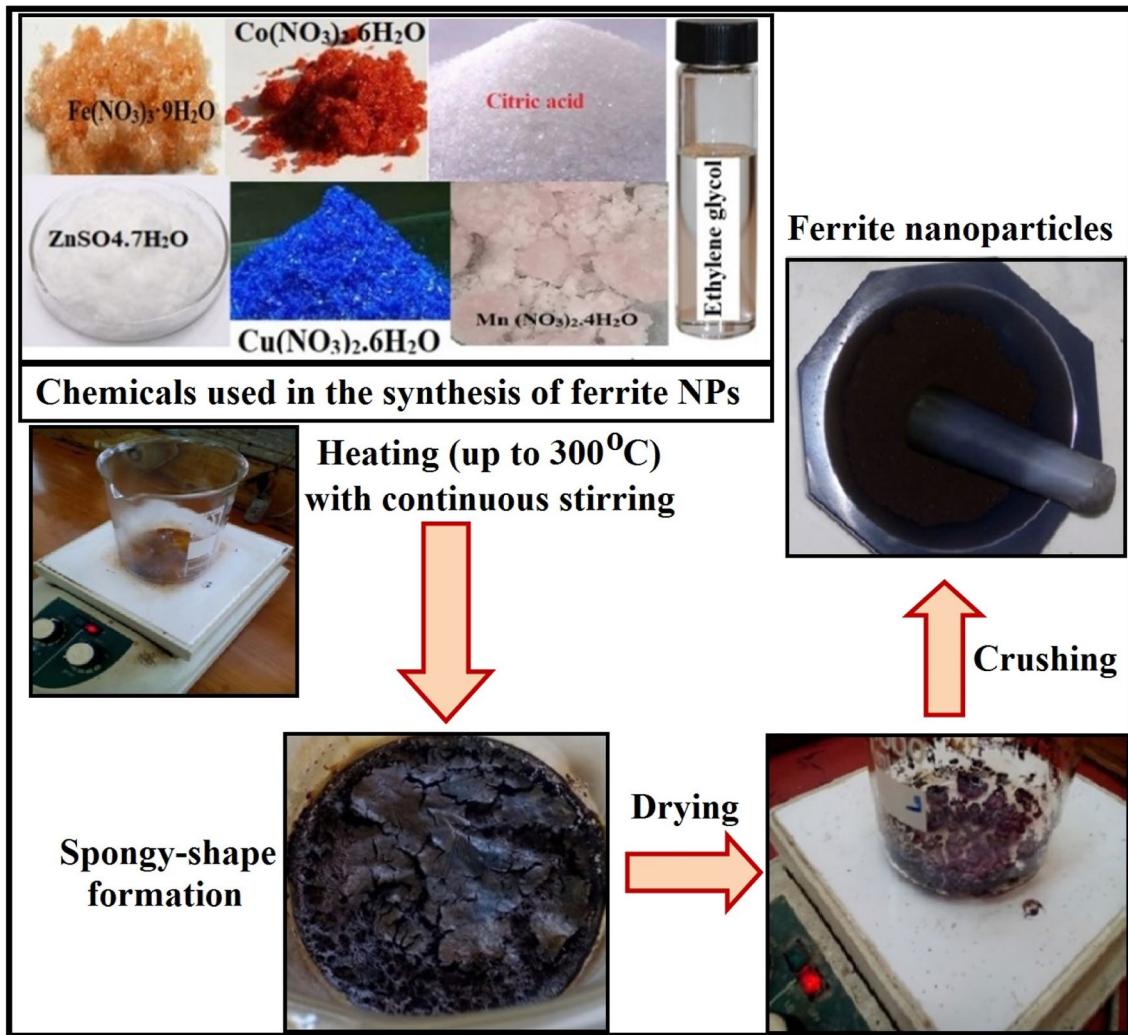
2.1 Materials

The chemicals used in the synthesis process were purchased from Sigma-Aldrich and were used without further purification; chemicals include $(\text{Fe}(\text{NO}_3)_3 \cdot 9\text{H}_2\text{O})$, $(\text{Co}(\text{NO}_3)_2 \cdot 6\text{H}_2\text{O})$, $(\text{ZnSO}_4 \cdot 7\text{H}_2\text{O})$, $(\text{Cu}(\text{NO}_3)_2 \cdot 6\text{H}_2\text{O})$, and $(\text{Mn}(\text{NO}_3)_2 \cdot 4\text{H}_2\text{O})$, citric acid ($\text{C}_6\text{H}_8\text{O}_7$, 99.57%), and ethylene glycol ($\text{C}_2\text{H}_6\text{O}_2$, 99.8%).

2.2 Methods

Our cobalt ferrites and metals' substituted cobalt ferrites were prepared according to the previously reported synthetic routes [12, 40–44]. Step-by-step formation stages of cobalt ferrite NPs via the eco-friendly and cost-effective sol–gel method are shown in Scheme 1.

Firstly, the stoichiometric amount of $(\text{Fe}(\text{NO}_3)_3 \cdot 9\text{H}_2\text{O})$, $(\text{Mn}(\text{NO}_3)_2 \cdot 4\text{H}_2\text{O})$, $(\text{Co}(\text{NO}_3)_2 \cdot 6\text{H}_2\text{O})$, $(\text{Cu}(\text{NO}_3)_2 \cdot 6\text{H}_2\text{O})$, and $(\text{Zn}(\text{SO}_4)_2 \cdot 7\text{H}_2\text{O})$ were dissolved in 30 ml of distilled water, separately. The mixture solution is stirred for 20 min. Then, citric acid solution was added to the above solution at 60°C under magnetic stirring. After that, 5 ml of ethylene glycol drop wisely used as a polymerization agent. The product solution was dried at 120°C to support for gel formation. Thereafter, the resulting gels were dehydrated and ground to achieve ferrite' powder.



Scheme 1 Synthetic stages of $\text{Co}_{1-x}\text{M}_x\text{Fe}_2\text{O}_4$ NPs ($\text{M} = \text{Zn}, \text{Cu}$ and Mn ; $x = 0.00$, and 0.50) using sol-gel method

2.3 Spectroscopic characterization of samples

The prepared ferrite NPs were characterized using many techniques including X-ray diffraction (XRD) spectroscopy (Shimadzu XRD-6000; Japan), recorded XRD patterns were obtained at room temperature with 2θ ranged from 17° to 90° . The used radiation source was $\text{Cu K}\alpha$ with a wavelength $\lambda = 0.15408$ nm, measurement recorded with a scan rate of $0.8^\circ/\text{min}$, operating voltage of 50 kV and current of 40 mA.

In order to confirm the preparation of the spinel ferrite phase, Fourier transform infrared spectroscopy (FTIR; Jasco, USA) is conducted over a wide range ($350\text{--}3000$ cm^{-1}). The FT-Raman spectrum was recorded using BRUKER RFS 27 FT-Raman spectrometer. The stoichiometry of the pristine ferrite NPs and metals substituted ferrite NPs samples is examined via employing the energy-dispersive X-ray analysis spectra (EDX), JEOL JSM-5600 LV, Japan. The information about the morphological shape and size of the

synthesized samples' is obtained by a high-resolution scanning electron microscopy (HRSEM), JEOL JSM-5600 LV, Japan).

Elemental composition analysis was performed using inductively coupled plasma optical emission spectrometer (ICP-OES) model Prodigy Prism High Dispersion (Teledyne Leeman ICP-OES USA). The obtained spectra were analyzed using a computer program based on the distribution technique analysis at ICP-OES measurement conditions as follows: 1.2 kW RF power, 20 L/min coolant gas flow, 0.3 L/min auxiliary gas flow, and 1 mL/min solution uptake rate.

The mean concentration of elements into our system was diluted by factor of 10,000 to be inside the range of measurement, and impurities from slandered materials used or atmosphere and tools of experiment were ignored as their concentration did not exceed 10 ppm.

Furthermore, shape and size of the synthesized ferrites NPs were investigated by HR-TEM analysis on

(JEOL-JEM-100 CX). Brunauer–Emmett–Teller (BET) method [10, 45–47] was used to describe the experimental specific surface area [48]. Surface area measurements were carried out via the surface area analyzer (Nova 3200 Nitrogen Physisorption Apparatus USA) with liquid N₂ as an adsorbate at −196 °C. The magnetization measurements have been performed at room temperature using a vibrating sample magnetometer (VSM of Lakeshore 7400) from −20 to +20 kG.

2.4 Data analysis

Rietveld refinement technique was used to analyze the XRD data on Full Prof Suite software. While, the mean size of crystallites (*D*) and the strain (ϵ) for Co_{1−*x*}M_{*x*}Fe₂O₄ NPs; M=Zn, Cu and Mn; *x*=0.00, and 0.50 were calculated by utilizing Williamson–Hall (W–H) method [49]. While the experimental lattice constant (*a*_{exp}), X-ray density (ρ_x), bulk density (ρ_b), the porosity percentage (*P*%), specific surface area (*S*; m²/g), and bond lengths of (*R*_A) and (*R*_B) were determined using the data obtained from Rietveld analyses [50–54].

3 Results and discussion

3.1 Structural study

Indeed, both bond stretching or bending are possible results of absorbing IR waves by different chemical compounds [55]. Accordingly, functional groups and molecular structure of the prepared metal-substituted cobalt ferrite NPs were analyzed using FTIR. FTIR spectra of Co_{1−*x*}M_{*x*}Fe₂O₄ NPs (M=Zn, Cu and Mn; *x*=0.00, and 0.50) are shown in Fig. 1.

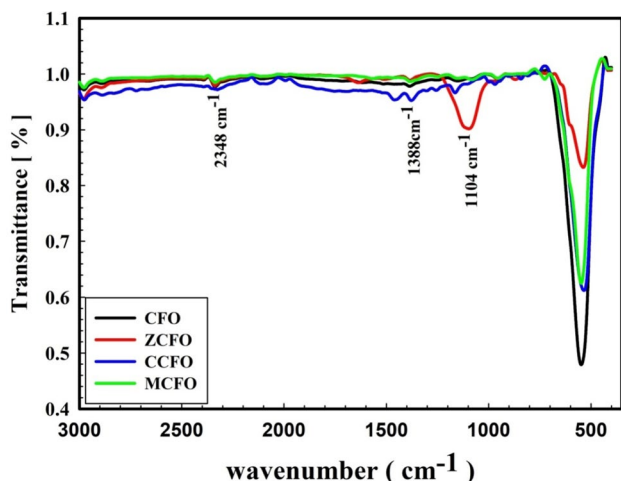


Fig. 1 The recorded FTIR spectra of the prepared Co_{1−*x*}M_{*x*}Fe₂O₄ NPs (M=Zn, Cu and Mn; *x*=0.00, and 0.50)

Table 1 The values of ν_1 and ν_2 and force constants for Co_{1−*x*}M_{*x*}Fe₂O₄ NPs (M=Zn, Cu and Mn; *x*=0.00, and 0.50)

Ferrite NPs	ν_1 (cm ^{−1})	F_t (N m ^{−1})	ν_2 (cm ^{−1})	F_o (N m ^{−1})
CFO	590.68	255.57	392.44	142.38
ZCFO	569.44	237.52	375.92	130.65
CCFO	588.32	253.53	380.64	133.95
MCFO	576.52	243.47	399.52	147.57

Two FTIR-active bands are common for spinel ferrites, known as ν_1 and ν_2 covering the range of (550–600 cm^{−1}) and (350–450 cm^{−1}), respectively. These two bands are attributed to oxygen bonds and metal ions in both A- and B-sites, respectively [56]. The values of ν_1 and ν_2 are presented in Table 1.

Table 1 reveals that active bands' positions shifts are corresponding to Co²⁺ cations and substituted metals' re-distribution over the sub-lattices [57]. The variation in ν_1 and ν_2 active vibration bands was due to the length of oxygen-metal ions bond, as it has long length in B-sites and short length in A-sites [58, 59].

In addition, Fig. 1 shows that the cubic spinel phase of the prepared samples has successfully been formed even after replacing cobalt ions of CFO ferrite by Zn, Cu, and Mn ions [60–63]. The characteristic bond of CFO NPs' formation appeared at 1104 cm^{−1}.

Moreover, nitrate groups' stretching vibration was recorded at a wave number of about 1388 cm^{−1}, i.e., the nitrate ions were present in the prepared samples. Additionally, the observed peaks at the wave number of 2350 cm^{−1} confirmed the existence of carbonyl groups [63]. Using FTIR data, the force constants were described as follows (Eq. 1) [64]:

$$F_{\nu_o} (\text{N m}^{-1}) = 4\pi^2 C^2 \nu_1^2 \nu_2^2 \mu \quad (1)$$

where F_t and F_o represent constants of both tetrahedral and octahedral sites, *C* is light velocity = 2.99 × 10⁸ m/s and μ is Fe³⁺ and O^{2−} ions' reduced mass which equals 2.060 × 10^{−26} kg

The variance of F_t and F_o for the prepared Co_{1−*x*}M_{*x*}Fe₂O₄ NPs (M=Zn, Cu and Mn; *x*=0.00, and 0.50) is shown in Table 1. From Table 1, one can observe that $F_t > F_o$, which may have an inverse relation with bond lengths [65, 66]. The constants of force (F_t and F_o) depend on Co²⁺ and substituted metals ions' ionic radii which vary according to their location at A- and B-sites [2].

Table 2 explains that R_A and R_B values were at the range of 1.8986–1.9145 Å and 2.0434–2.0606 Å, respectively. Bond lengths' variation can be attributed to the disparity in the ionic radii of metals replacing cobalt in the nanocrystalline samples [67].

Table 2 The average crystallite size, strain, experimental lattice parameter, X-ray density, Bulk density, and porosity of $\text{Co}_{1-x}\text{M}_x\text{Fe}_2\text{O}_4$ NPs (M = Zn, Cu and Mn; $x = 0.00$, and 0.50)

Ferrite NPs	$D_{\text{W-H}}$ (nm)	Straine	Lattice parameter a_{exp} (Å)	X-ray density ρ_x (g cm^{-3})	Bulk density ρ_b (g cm^{-3})	Percentage porosity (P %)	Bond lengths (Å)	
							R_A	R_B
CFO	25.1036	− 0.0004	8.371	4.8280	4.6891	2.87	1.8986	2.0434
ZCFO	11.7872	− 0.00080	8.441	4.7736	3.0255	36.62	1.9145	2.0606
CCFO	14.0410	− 0.00140	8.385	4.8515	4.4664	7.93	1.9018	2.0468
MCFO	33.5058	− 0.00061	8.414	4.7137	4.1401	12.16	1.9084	2.0540

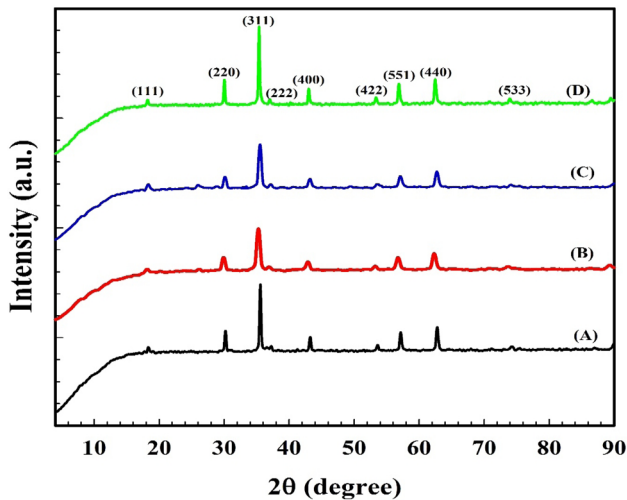


Fig. 2 X-ray diffraction patterns of (a) CFO, (b) ZCFO, (c) CCFO, and (d) MCFO NPs

Crystalline structure and phase formation of metals-substituting CFO NPs have been analyzed using XRD. Figure 2 reveals the XRD patterns of the synthesized $\text{Co}_{1-x}\text{M}_x\text{Fe}_2\text{O}_4$ NPs (M = Zn, Cu, and Mn; $x = 0.00$, and 0.50). Main peaks were observed at 2θ of 18.28° , 30.12° , 35.54° , 37.12° , 43.13° , 53.41° , 56.89° , 62.62° , and 73.75° , corresponding to the metals substituted CFO NPs and specified with the space group of Fd3m. These results well matched the spinel cubic phase of CFO ferrites, JCPDS (Card No. 22-1086) [68].

Usually, diffraction peaks' shift to the lower or higher angles occurs because of the changes with lattice constants. The peak observed at $2\theta = 35.54^\circ$ and (311) plane orientation was shifted to the lower angles of diffraction for cation-substituted CFO NPs (Fig. 3).

This shift can be explained according to unit cell extension and lattice constant enhancement as shown in Table 2. Lattice constant's variation for CFO NPs and other samples can be due to ionic radii variation of substituted metals and preferred site occupancy, where $r(\text{Zn}^{2+})$, $r(\text{Cu}^{2+})$, $r(\text{Mn}^{2+})$, and $r(\text{Co}^{2+})$ were taken as follows: (tetra: 0.60 and octa: 0.74 Å), (tetra: 0.57 and octa: 0.73 Å), (tetra: 0.58 and octa: 0.72 Å), and (tetra: 0.58 and octa: 0.745 Å), respectively [69].

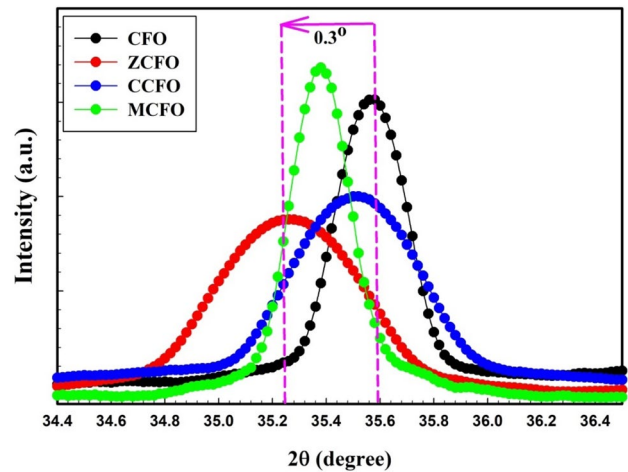


Fig. 3 XRD patterns at $2\theta = 35.54^\circ$ for (311) plan of $\text{Co}_{1-x}\text{M}_x\text{Fe}_2\text{O}_4$ NPs (M = Zn, Cu, and Mn; $x = 0.00$, and 0.50)

These results were in a good agreement with the previously published data [19, 70, 71].

Herein, to reveal various aspects such as structure of the metals substituted cobalt ferrite samples, the Rietveld refinements were carried out (Figure S1; provided in the supplementary material).

The observed intensities, the calculated intensities, and the difference between observed and calculated intensities are presented as red, black, and blue lines, respectively. Fd3m space group's allowed Bragg positions were represented as vertical lines.

All recorded peaks enabled Bragg 2θ positions. From occupancy variance, we have seen that Co^{2+} ion occupy both A-site and B-site. Therefore, we can assume that the CFO NPs is in a random spinel composition. The investigation for site occupancy to standard CFO NPs reveals that 10% of A-site has been occupied by the Co^{2+} ions and the remaining 90% A-sites by Fe^{3+} ions.

So, the chemical formula for CFO NPs is $(\text{Fe}_{0.90}\text{Co}_{0.10})[\text{Fe}_{1.10}\text{Co}_{0.90}]\text{O}_4$, the occupied A- and B-sites were represented by the cations in the round and square brackets, respectively [72],

Whereas for ZCFO NPs, the cation distribution has been estimated from the knowledge that Co^{2+} ions have a trend to occupy both A- and B-sites. In contrast, the Zn^{2+} ions are preferred to occupy the A-site. The site occupancy examination for standard ZCFO NPs exposes that 9% A-site has been occupied by the Co^{2+} ions, 41% A-site has been occupied by the Fe^{3+} ions and the remaining 50% A-site occupied by Zn^{2+} ions. Therefore, the chemical description for this sample is $(\text{Fe}_{0.41}\text{Co}_{0.09}\text{Zn}_{0.50})[\text{Fe}_{1.59}\text{Co}_{0.41}]\text{O}_4$ [18].

Furthermore, Co^{2+} ions, Cu^{2+} ions, and Fe^{3+} ions occupied both A- and B-sites as revealed by Rietveld analysis for CCFO NPs [38, 73]. The site occupancy analysis of MCFO sample reveals that the tetrahedral site has been occupied by the ions Co, Mn, and Fe with the ratios 5%, 40%, and 55%, respectively. Hence, the chemical formula for this sample is $(\text{Fe}_{0.55}\text{Co}_{0.05}\text{Mn}_{0.40})[\text{Fe}_{1.45}\text{Co}_{0.45}\text{Mn}_{0.10}]\text{O}_4$. This result agrees well with the reference [70].

From Rietveld fitted XRD patterns, the present samples have kept on cubic spinel phase. However, small peak was observed in CCFO NPs at $2\theta \approx 33.25^\circ$ corresponding to the tetragonal structure of CCFO NPs. Jahn–Teller' effect caused this tetragonal distortion of Cu^{2+} ions which occupied B-sites of the copper cobalt ferrite in a high content [38, 70, 72–75].

From reflection broadening, both crystallite size and micro-strain can be defined by the elegant Williamson–Hall (W-H) method. As explained in Figure S2 (provided in the supplementary material), W-H plots of the prepared $\text{Co}_{1-x}\text{M}_x\text{Fe}_2\text{O}_4$ NPs ($\text{M} = \text{Zn}, \text{Cu}$ and Mn ; $x = 0.00$, and 0.50) were used to determine the average size of crystallites, $D_{\text{W-H}}$, and the micro-strain for the tested samples. According to our calculations and as depicted in Table 2, the crystallite size ranges from 11.787 nm to 33.505 nm depending on the cations [49]. In the same context, the investigated samples exhibited compressive strain [76].

The values of X-rays' density, bulk density, and porosity (P) of the prepared $\text{Co}_{1-x}\text{M}_x\text{Fe}_2\text{O}_4$ NPs ($\text{M} = \text{Zn}, \text{Cu}$ and Mn ; $x = 0.00$, and 0.50) are shown in Figure S3 (provided in the supplementary material). Figure S3 clearly revealed that porosity behaves on contrary to the bulk density. Besides ρ_x values were lied in the range of (4.7137–4.8280 g/cm^3), which were found to be bigger than the values of ρ_b (3.0255–4.6891 g/cm^3).

This observation can be explained by enormous pores that are unique to present samples (2.87–36.62)%. These pores' formation was attributed to the liberation of huge gases' volumes during the preparation process [77]. The variation in ferrites' porosities can be linked to copper ions' density that equals (8.96 g/cm^3), which is larger than that of cobalt ions (8.86 g/cm^3), zinc ions (7.14 g/cm^3), and manganese ions (7.43 g/cm^3). Similar results have been reported previously [42, 43, 78].

Phase investigation of the prepared samples was performed using Raman analyses. The metallic cations of cobalt ferrite samples have the possibility of occupying two positions forming either octahedron or tetrahedron by binding with six O_2 anions or four O_2 anions, respectively [79]. This structure gives many modes, among them, 5 modes are Raman-active as follows ($\text{A}1\text{g} + 1\text{Eg} + 3\text{T}2\text{g}$) [79].

Raman spectra of the prepared samples are shown in Fig. 4. It can be revealed that, T2g (1) mode appeared at 192 cm^{-1} , e.g., mode was recorded at 298.5 cm^{-1} , T2g (2) mode was observed at 454.6 cm^{-1} , and T2g (3) mode was recorded at 541.4 cm^{-1} , which can be attributed to the vibration of the spinel structure [80].

Indeed, T2g modes are likely due to asymmetric stretching of O_2 anions, e.g. mode occurs due to bending of O_2 anions. In CFO sample, cobalt and iron ions occupy its octahedral site, while its tetrahedral site is busy with iron ions only. As a result of the variance in cobalt and iron's ionic radii, the bond distances of both Fe–O and Co–O are redistributed between both sites and caused a doublet-like structure [81].

Fe–O and M–O ($\text{M} = \text{Zn}, \text{Mn}$ and Cu) stretching vibrations were observed at 607 cm^{-1} and 678 cm^{-1} corresponding to $\text{A}1\text{g}$ (2) and $\text{A}1\text{g}$ (1) modes, respectively [81]. Almost the same Raman peaks were observed by the prepared transition metal-substituted cobalt ferrite samples. However, some changes in the intensity and small peak shift were recorded which were attributed to the relatively larger atomic mass of Mn, Zn, and Cu ions compared with Co ions and the high cation disorder induced by their substitution [79].

The EDX analysis provides many ways to track samples' composition, purity, and elements' mapping. Figure 5 shows the EDX spectra of the prepared $\text{Co}_{1-x}\text{M}_x\text{Fe}_2\text{O}_4$ NPs ($\text{M} = \text{Zn}, \text{Cu}$ and Mn ; $x = 0.00$, and 0.50).

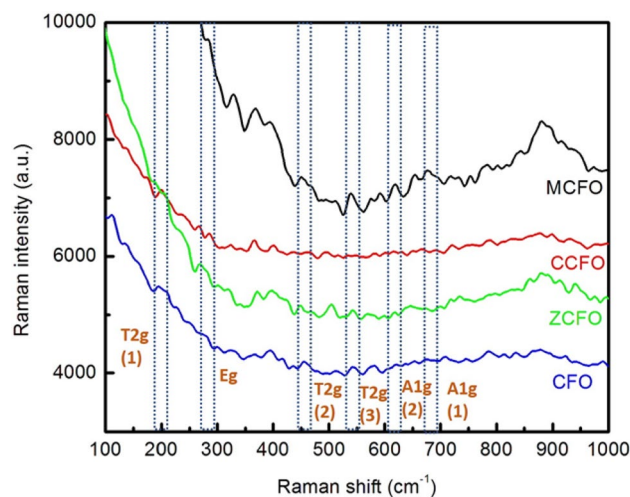


Fig. 4 Raman spectra of the prepared $\text{Co}_{1-x}\text{M}_x\text{Fe}_2\text{O}_4$ NPs ($\text{M} = \text{Zn}, \text{Cu}$, and Mn ; $x = 0.00$, and 0.50)

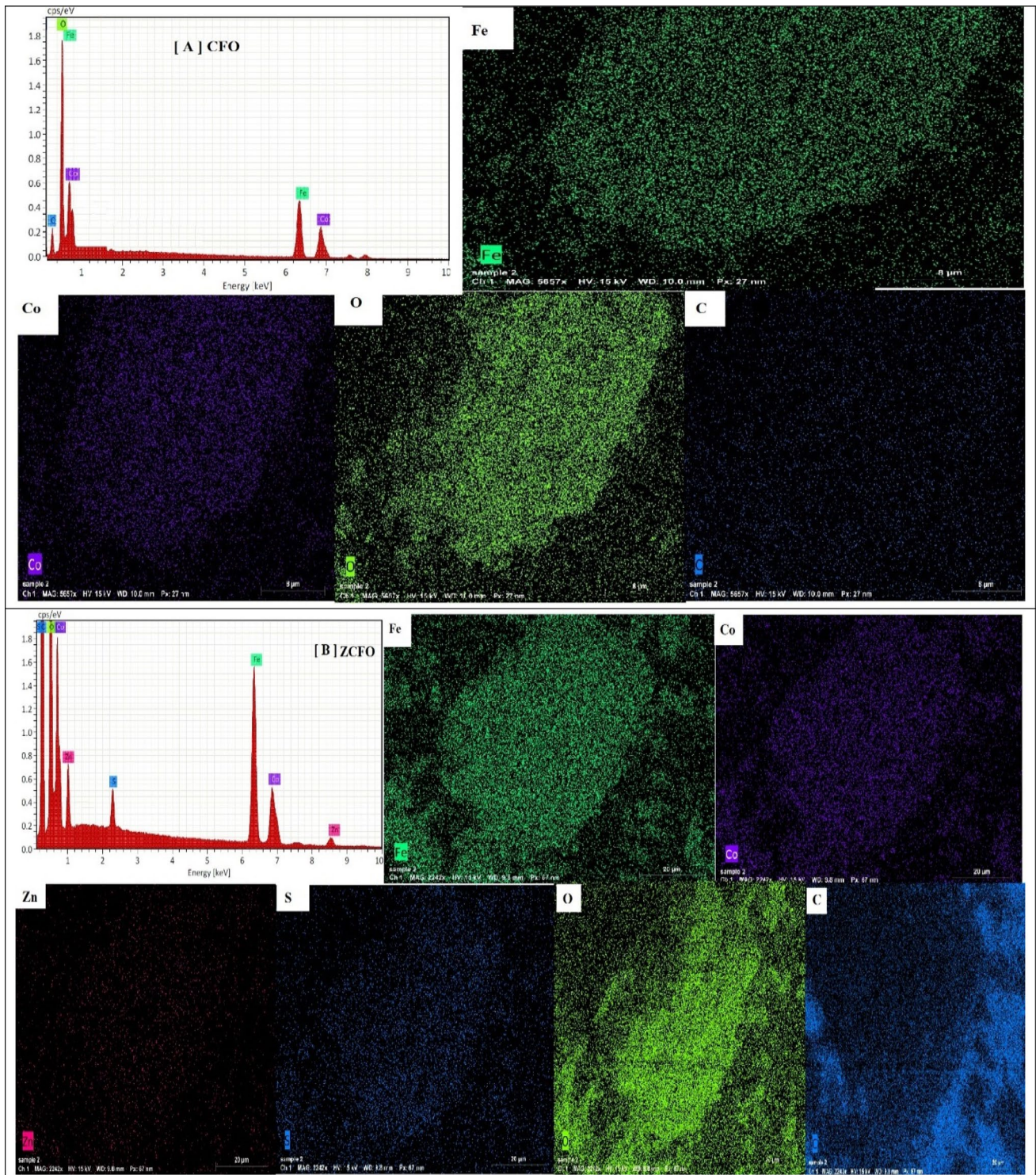


Fig. 5 EDX elemental measurements and SEM/EDX mapping for **a** CFO, **b** ZCFO, **c** CCFO, and **d** MCFO NPs

It is clearly observed that, Zn, Cu, Mn, Co, O, and Fe elements were existed with various stoichiometric ratios. The

carbon ratios that appear in the spectra can be attributed to using the citric acid and/or ethylene glycol [76, 82].

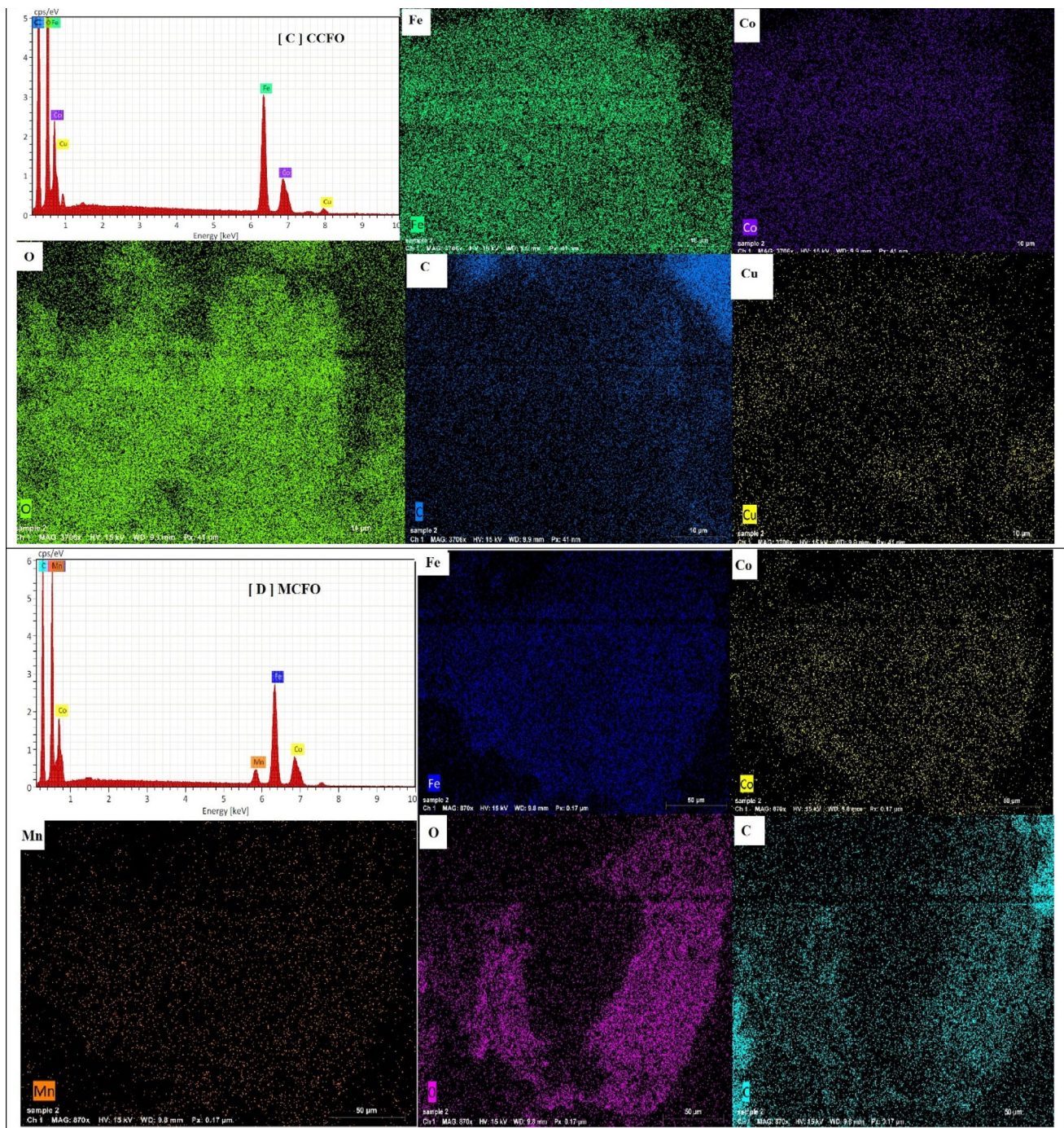


Fig. 5 (continued)

EDS data confirmed that production of pure nanostructured $\text{Co}_{1-x}\text{M}_x\text{Fe}_2\text{O}_4$ NPs ($\text{M} = \text{Zn}, \text{Cu},$ and $\text{Mn}; x = 0.00,$ and 0.50) without any impurities except for ZCFO sample, where we found a small fraction of sulfur ions that

were attributed to residues of the sulfate group [83]. These results alongside with XRD and FTIR results confirm the

successful preparation of spinel cubic phase structure of metals substituted CFO NPs.

Table 3 ICP-OES elemental analyses for $\text{Co}_{1-x}\text{M}_x\text{Fe}_2\text{O}_4$ NPs (M = Zn, Cu and Mn; $x = 0.00$, and 0.50)

ICP-OES					
Element	CFO	ZCFO	CCFO	MCFO	Average RSD
(PPM) $\times 10^5$					
Fe	45.87	38.1	47.11	52.02	± 0.56
Co	26.9	11.05	13.04	14.07	± 0.54
C	–	–	–	–	–
Zn	–	11.03	–	–	± 0.65
S	–	1.92	–	–	± 1.3
Cu	–	–	11.08	–	± 0.43
Mn	–	–	–	11.02	± 0.47

The ICP-OES was used to examine the elemental composition of metals M^{2+} ions substituted CFO NPs as illustrated in Table 3 [84]. This table confirmed the presence of Mn, Zn, Fe, Cu, and Co cations. Moreover, it is clear that metals concentration was increased at the expense of Co^{2+} ions in the prepared samples [85]. These results well matched our EDX analysis [86].

On the other hand, Fig. 6 presents the HR-TEM images of all samples. The spherical shape of particles was obvious; also, the images illustrated that the particles were in the nanometer range.

The pure CFO ferrite had a uniform shape and a size of around 27.0 nm. Then, the particle size was sharply decreased for ZCFO NPs reaches about 10.0 nm and increased to reach 15.0 nm for CCFO NPs.

Furthermore, the NPs looked like to be much larger and were more agglomerated for MCFO NPs (~ 33.0 nm)

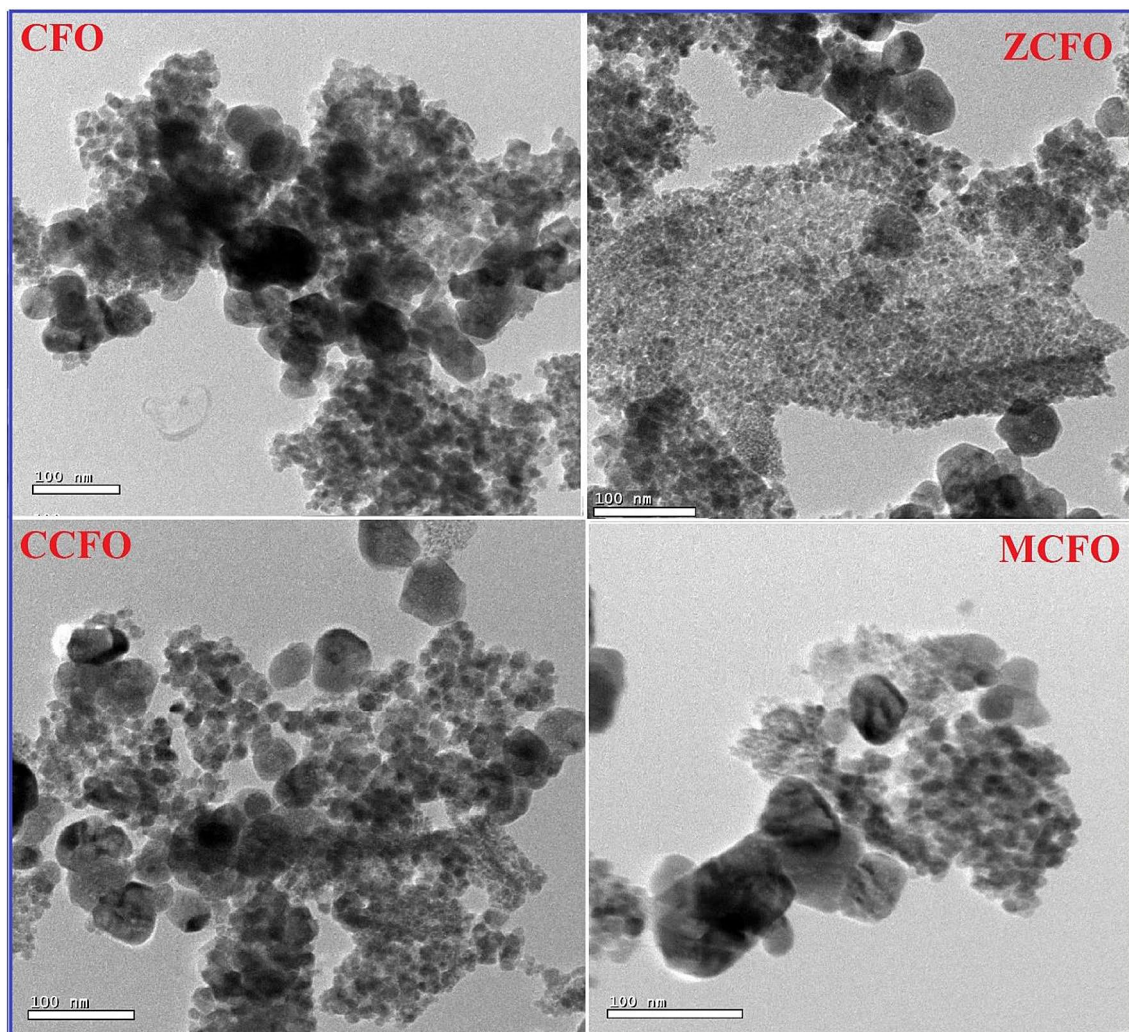


Fig. 6 TEM images of the prepared $\text{Co}_{1-x}\text{M}_x\text{Fe}_2\text{O}_4$ NPs (M = Zn, Cu and Mn; $x = 0.00$, and 0.50)

[43]. These results were in a great conformity with those estimated from the XRD analysis [86–88].

Ferrites' electrical and magnetic properties are specific surface area and grain size dependant, as the chemical and physical phenomena controlled by surface porosity and electrons conduction occur at ferrites' surface. To further investigate the adsorption mechanism of $\text{Co}_{1-x}\text{M}_x\text{Fe}_2\text{O}_4$ NPs; (M = Zn, Cu and Mn; $x = 0.00$, and 0.50), the analysis was performed utilizing BET procedure for all samples.

The nitrogen adsorption–desorption isotherms of $\text{Co}_{1-x}\text{M}_x\text{Fe}_2\text{O}_4$ NPs; (M = Zn, Cu and Mn; $x = 0.00$, and 0.50) are given in Fig. 7. The isotherms are presented in Fig. 7 and revealing class IV behavior, as expected for a mesoporous material [89].

Similar behavior in our previous work was detected [40, 90]. Moreover, it is obvious from this figure that the ZCFO NPs had the highest specific surface area of $26.87 \text{ m}^2/\text{g}$ and this outcome data were in good match with the surface area value of metal oxides [91].

Also, the specific surface area (S) of MCFO reaches $24.40 \text{ m}^2/\text{g}^{-1}$, which is higher than of those obtained for CFO NPs ($7.31 \text{ m}^2/\text{g}^{-1}$), and CCFONPs ($5.01 \text{ m}^2/\text{g}^{-1}$). The higher value of the specific surface area for ZCFO NPs is attributed to the small crystallite size and huge porosity. Similar behavior is showed in previous research [12, 24, 40, 92].

3.2 Elastic properties

Stiffness constants' (C_{11} and C_{12}) values can be determined by utilizing X-ray and FTIR data [65, 93–96]. Figure 8 illustrates that constants of stiffness, C_{11} and C_{12} , have decreased by the substitution process in CFO NPs owing to increment of the lattice constant.

The stiffness constants are influenced by the force constants depending on the lengths of the bond created between the atoms [97]. The values of stiffness constant, C_{11} , decreased from 237.70 GPa for CFO NPs to 218.09 GPa for ZCFO NPs, as well as C_{12} decreased from 1.5312 GPa for CFO NPs to 0.9742 GPa for ZCFO NPs.

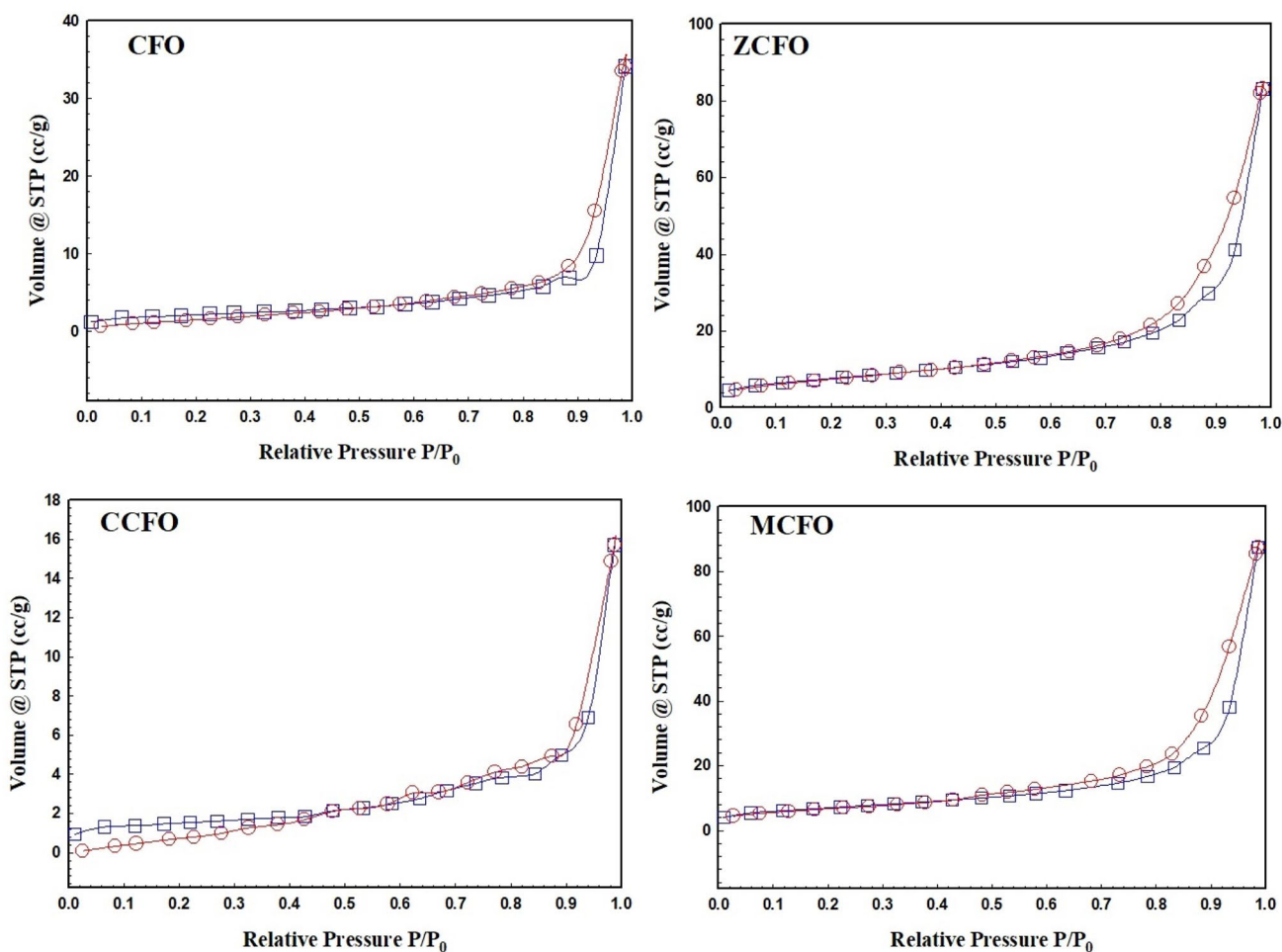


Fig. 7 BET nitrogen spectra of the prepared $\text{Co}_{1-x}\text{M}_x\text{Fe}_2\text{O}_4$ NPs (M = Zn, Cu and Mn; $x = 0.00$, and 0.50)

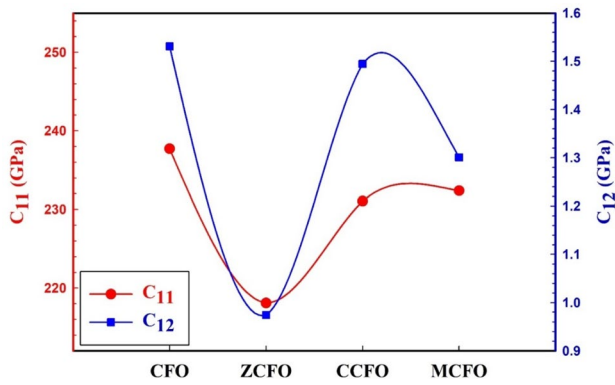


Fig. 8 The stiffness constants, C_{11} and C_{12} for $\text{Co}_{1-x}\text{M}_x\text{Fe}_2\text{O}_4$ NPs ($\text{M}=\text{Zn}$, Cu , and Mn ; $x=0.00$, and 0.50)

In addition, bulk modulus (B), rigidity modulus (G), and Young's modulus (E) can be calculated by the stiffness constants as follows (Eqs. 2–4) [60].

$$B = \frac{1}{3}[C_{11} + 2C_{12}] \quad (2)$$

$$E = \frac{[C_{11} - C_{12}][C_{11} + 2C_{12}]}{[C_{11} + C_{12}]} \quad (3)$$

$$G = \frac{E}{2[\sigma + 1]} \quad (4)$$

The variation in elastic moduli B , E , and G for CFO NPs and $\text{Co}_{0.5}\text{M}_{0.5}\text{Fe}_2\text{O}_4$ NPs; $\text{M}=\text{Zn}$, Cu , and Mn is presented in Fig. 9. It was clearly confirmed that all moduli were cation-dependent. Figure 9 illustrates that the value of bulk modulus B decreases from 80.25 GPa for CFO NPs to 73.34 GPa for ZCFO NPs. In addition, the moduli E and G showed similar behaviors.

This variance can be attributed to that the bonds for inter-atomic which are created between different atoms in

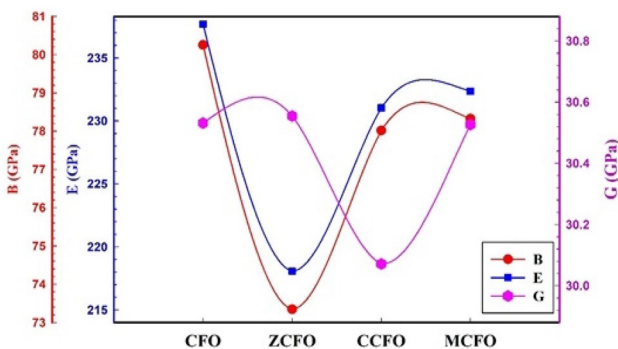


Fig. 9 The elastic moduli for $\text{Co}_{1-x}\text{M}_x\text{Fe}_2\text{O}_4$ NPs ($\text{M}=\text{Zn}$, Cu , and Mn ; $x=0.00$, and 0.50)

the system are weakened utilizing the substituted metals. Additionally, the values of elastic moduli depend on porosities of the ferrite samples [98].

The elastic moduli for ferrites NPs are depended on densities and subsequently on Poisson ratio. Our samples are porous; therefore, the elastic modulus of non-porous NPs will be greater than those estimated in our samples [96, 99]. Hence, the velocities of transverse (V_s) and longitudinal (V_l) wave can be written as (Eqs. 5–8) [2]:

$$V_s = [G_0/\rho_x]^{1/2} \quad (5)$$

$$V_l = [C_{11}/\rho_x]^{1/2} \quad (6)$$

where G_0 is rigidity modulus with correct zero porosity. According to V_s and V_l , we obtain the mean velocity V_m and the Debye temperature θ_D [100–102]:

$$V_m = \left[\frac{1}{3} \left(\frac{2}{V_s^3} + \frac{1}{V_l^3} \right) \right]^{-1/3} \quad (7)$$

$$\theta_D = \frac{h}{k} \left[\frac{3N_A \rho_x q}{4\pi M} \right]^{1/3} \times V_m \quad (8)$$

where q is number of atoms in the unit cell (in cubic spinel system equals 7).

Further, we can determine the Debye temperature (θ_l) using the wave number of FTIR bands [97, 100]. Figure 10 illustrates the variation of Debye temperature for $\text{Co}_{1-x}\text{M}_x\text{Fe}_2\text{O}_4$ NPs ($\text{M}=\text{Zn}$, Cu and Mn ; $x=0.00$, and 0.50). It is seen from this figure that the (θ_D) and (θ_l) are in a good conformity with each other. We observed that the Debye temperature obeys a similar behavior to that of B and

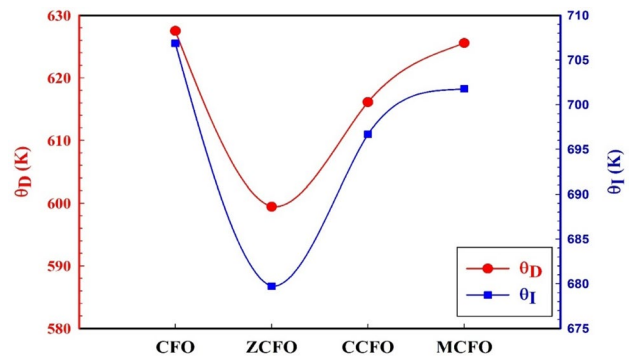


Fig. 10 The variation of Debye temperature estimated from elastic (θ_D) and infrared (θ_l) data for $\text{Co}_{1-x}\text{M}_x\text{Fe}_2\text{O}_4$ NPs ($\text{M}=\text{Zn}$, Cu and Mn ; $x=0.00$, and 0.50)

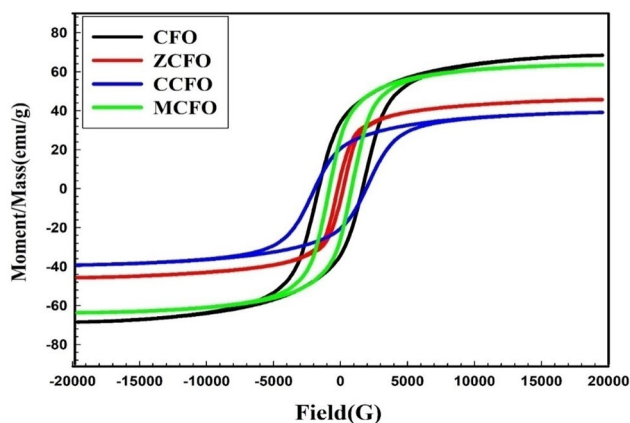


Fig. 11 Magnetization-field (M - H) hysteresis loops for $\text{Co}_{1-x}\text{M}_x\text{Fe}_2\text{O}_4$ NPs ($M = \text{Zn}, \text{Cu}, \text{and Mn}; x = 0.00, \text{ and } 0.50$)

Table 4 Saturation magnetization (M_s), remanence magnetization (M_r), coercivity (H_c), remanence ratio (M_r/M_s) of $\text{Co}_{1-x}\text{M}_x\text{Fe}_2\text{O}_4$ NPs; ($M = \text{Zn}, \text{Cu}, \text{ and Mn}; x = 0.00, \text{ and } 0.50$)

Ferrite NPs	M_s (emu/g)	M_r (emu/g)	H_c G	M_r/M_s
CFO	68.419	34.014	1617.30	0.4972
ZCFO	45.687	6.149	213.93	0.1346
CCFO	39.128	20.476	1914.80	0.5233
MCFO	63.584	25.657	819.30	0.4034

G moduli, which confirms the compatibility between the reported elastic parameters and the porosity [2].

3.3 Magnetic properties

Metal ions' substitution in CFO NPs has a significant impact on the magnetic behavior of the tested samples as shown by the hysteresis loops (Fig. 11). The magnetization saturation and coercivity values are determined and summarized in Table 4 [103, 104].

A typical S-shaped curve for ZCFO NPs has been observed indicating super paramagnetic character. Ferri-magnetism to paramagnetism transformation was attributed to the anti-parallel alignment's reduction of two distinct magnetic ions (Fe^{3+} and Co^{2+}) at A- and B-sites with the substituted Zn^{2+} ion [105].

In other words, the Zn^{2+} ($0 \mu_B$) ions have more tended to occupy A-sites while the Fe^{3+} ions migrate from A-sites to B-sites. Therefore, as Zn^{2+} ion contents in CFO NPs sample increase, the occupancy of Fe^{3+} ions is declined in the A-sites and is increased in the B-sites.

The observed saturation magnetization (M_s) is drastically decreased from 68.419 emu/g for CFO NPs sample to 45.687 emu/g for ZCFO NPs sample, which in good agreement with earlier research [106].

In the case of Cu^{2+} ions substituted Co^{2+} ions, the copper ions have strongly preferred octahedral site occupancy leading to the reduction of the super-exchange interaction between the A- and B-sites. More precisely, when Cu^{2+} ions substituted Co^{2+} ions, the Fe^{3+} and Co^{2+} ions migrated from B-site to A-site lead to reducing the magnetization of the B-site and subsequently the net magnetization was reduced [74].

According to consulting Hund's rule, we replace the Cu^{2+} ($1 \mu_B$) in the place of Fe^{3+} ($5 \mu_B$) and Co^{2+} ($3 \mu_B$) ions in B-sites, which leads to reducing the net magnetic moment of CCFO NPs sample (39.128 emu/g). Similar results are previously reported in reference [107].

Finally, in the case substituted Co^{2+} by Mn^{2+} ions and according to consulting Hund's rule, the atomic magnetic moment of the, Fe^{3+} ($5 \mu_B$), Co^{2+} ($3 \mu_B$), and Mn^{2+} ($4.5 \mu_B$). From the above turned out to be that magnetization of Mn^{2+} ions is higher than Co^{2+} ions, additionally the distribution of cationic has a prevailing effect on the total magnetization. The Mn^{2+} has been strongly preferred to occupy A-site, which leads to increasing the magnetization of A-sites.

Spinel system's net magnetic moment is the difference between the magnetic moments of B- and A-sites. Consequently, the substitution Co^{2+} by Mn^{2+} ions reduces the net magnetization for the MCFO NPs sample (63.584 emu/g), in good agreement with the previous studies [108, 109].

The magnetic parameters of spinel ferrites NPs are highly affected by the numerous factors such as porosity, homogeneity, morphology, density, and distribution of cations at lattice sites [7]. The determined values of the remanent magnetization for ZCFO NPs, CCFO NPs, and MCFO NPs are approximately 6.149, 20.476, and 25.657 emu/g, respectively.

These results are smaller than that acquired for CFO NPs (34.014 emu/g). Moreover, the determined coercive field for CCFO NPs ($H_c = 1914.85$ G) is higher than that acquired for other samples, where the value of coercive, H_c , for CFO NPs, ZCFO NPs, and MCFO NPs is 1617.30 G, 213.93 G, and 819.34 G, respectively.

Additionally, spinel ferrite NPs' coercivity depends on many parameters such as internal strains, particle size, lattice imperfections, magneto-crystalline anisotropy, dislocations, and secondary phases [110].

The remanent magnetization ratio (M_r/M_s) decreases from 0.5233 for CCFO NPs sample to 0.1346 for ZCFO NPs sample. This result refers to the reduction of the anisotropic behavior within the studied ferrite samples [24].

Our results highly support the application of metals substituted CFO NPs in the areas of photo-catalysis and bio-medicine [111, 112]. The B-sites have a significant role in the catalytic producer, due to the presence of large distances from the each other whereas the A-sites catalytically inactive. The substitution of the Fe^{3+} ions with the Zn^{2+} , Cu^{2+} ,

and Mn^{2+} ions caused defects in the lattice of the spinel ferrite system. The presence of defects improved the efficiency of photo-catalytic degradation [113].

4 Conclusion

Facile and eco-friendly sol–gel method was used to prepare metals substituted cobalt ferrite CFO NPs ($\text{Co}_{1-x}\text{M}_x\text{Fe}_2\text{O}_4$ NPs; $\text{M} = \text{Zn}, \text{Cu}$, and Mn ; $x = 0.00$, and 0.50). X-ray diffraction and infrared spectra indicated the presence of cubic spinel phase. The isotherms for $\text{Co}_{0.5}\text{M}_{0.5}\text{Fe}_2\text{O}_4$ NPs; $\text{M} = \text{Zn}, \text{Cu}$, and Mn reveal class IV behavior, as expected for a mesoporous material. The specific surface area of ZCFO NPs is $26.87 \text{ m}^2\text{g}^{-1}$ which is higher than those obtained for MCFO NPs ($24.40 \text{ m}^2\text{g}^{-1}$), CFO NPs ($7.31 \text{ m}^2\text{g}^{-1}$), and CCFO NPs ($5.01 \text{ m}^2\text{g}^{-1}$) which attributed to the small crystallite size and huge porosity. The stiffness constants and elastic moduli are decreased with replacement Zn^{2+} ($0 \mu_{\text{B}}$), Cu^{2+} ($1 \mu_{\text{B}}$), Mn^{2+} ($4.5 \mu_{\text{B}}$) ions to Co^{2+} ions ($3 \mu_{\text{B}}$) in the host CFO NPs. Despite the convergence of the values of ionic radii of the substituted ions, however, the magnetization is strongly influenced due to the difference of the magnetic moment of the substituted ions. The recorded hysteresis loops confirmed that replacing cobalt ions with Zn^{2+} , Cu^{2+} , and Mn^{2+} ions has an extreme effect on the magnetic properties of CFO NPs. The metallic cations of cobalt ferrite samples have the possibility of occupying two positions forming either octahedron or tetrahedron by binding with six O_2 anions or four O_2 anions, respectively. EDX data confirmed the production of pure nanostructured ferrites without any impurities. ICP-OES confirmed the presence of Mn , Zn , Fe , Cu , and Co cations. Moreover, it is clear that metals' concentration was increased at the expense of Co^{2+} ions in the prepared samples. HR-TEM images of the prepared ferrite NPs reveal the spherical shape in the nanometer range. We think that the observed high surface area and reasonable saturation magnetization and coercivity values of our samples make them promising materials in screen-printed electrodes, biomedical, and photo-catalytic applications. Some of the challenges need to overcome in the future are understanding the procedures of the generation of these nanomaterials and scaling-up engineering investment required to the various purposes. Regulating equipment, agglomeration of the nanomaterials, and composite structural design are usually the principal obstetrical for scaling-up engineering.

Acknowledgements The authors acknowledge Materials Science Unit, National Center for Radiation Research and Technology, Egypt, for supporting this study under the project “Synthesizing and Characterizations of Nanostructured Magnetic Materials.” Finally, the author Gharieb S. El-Sayyad would like to thank Prof. Mohamed Gobara and Chemical Engineering Department, Military Technical College (MTC),

Egyptian Armed Forces, Cairo, Egypt for the continued support during this study.

Compliance with ethical standards

The authors declare that they have no conflict of interest.

References

- J. Jadhav et al., Structural and magnetic properties of nanocrystalline NiZn ferrites: in the context of cationic distribution. *J. Alloys Compd.* **696**, 28–41 (2017)
- N. Abu-Elsaad, Elastic properties of germanium substituted lithium ferrite. *J. Mol. Struct.* **1075**, 546–550 (2014)
- A.A. Khan et al., Structural, magnetic and magnetocaloric properties of $\text{CoFe}_{2-x}\text{Mo}_x\text{O}_4$ ($0.0 \leq x \leq 0.3$) ferrites. *Ceram. Int.* **43**(9), 7088–7093 (2017)
- A.-H. El Foulani et al., Effect of surfactants on the optical and magnetic properties of cobalt-zinc ferrite $\text{Co}_{0.5}\text{Zn}_{0.5}\text{Fe}_2\text{O}_4$. *J. Alloys Compd.* **774**, 1250–1259 (2019)
- M.T. Farid et al., Synthesis, electrical and magnetic properties of Pr-substituted Mn ferrites for high-frequency applications. *J. Electron. Mater.* **46**(3), 1826–1835 (2017)
- P. Chand, S. Vaish, P. Kumar, Structural, optical and dielectric properties of transition metal (MFe_2O_4 ; $\text{M} = \text{Co}, \text{Ni}$ and Zn) nanoferrites. *Physica B* **524**, 53–63 (2017)
- M.N. Akhtar et al., Structural, spectral, dielectric and magnetic properties of $\text{Ni}_{0.5}\text{Mg}_x\text{Zn}_{0.5-x}\text{Fe}_2\text{O}_4$ nanosized ferrites for microwave absorption and high frequency applications. *Ceram. Int.* **43**(5), 4357–4365 (2017)
- R. Sharma et al., Ferrimagnetic Ni^{2+} doped Mg-Zn spinel ferrite nanoparticles for high density information storage. *J. Alloys Compd.* **704**, 7–17 (2017)
- C. Wei et al., Hierarchical porous $\text{NiCo}_2\text{O}_4/\text{CeO}_2$ hybrid materials for high performance supercapacitors. *Inorg. Chem. Front.* **5**(12), 3126–3134 (2018)
- C. Wei et al., Mesoporous nickel cobalt manganese sulfide yolk–shell hollow spheres for high-performance electrochemical energy storage. *Inorg. Chem. Front.* **6**(7), 1851–1860 (2019)
- Z. Yan, J. Luo, Effects of CeZn co-substitution on structure, magnetic and microwave absorption properties of nickel ferrite nanoparticles. *J. Alloys Compd.* **695**, 1185–1195 (2017)
- M.I.A. Abdel Maksoud et al., Synthesis and characterization of metals-substituted cobalt ferrite [$\text{M}_x\text{Co}_{(1-x)}\text{Fe}_2\text{O}_4$; ($\text{M} = \text{Zn}, \text{Cu}$ and Mn ; $x = 0$ and 0.5)] nanoparticles as antimicrobial agents and sensors for Anagrelide determination in biological samples. *Mater. Sci. Eng. C* **92**, 644–656 (2018)
- G. Padmapriya et al., Spinel $\text{Ni}_x\text{Zn}_{1-x}\text{Fe}_2\text{O}_4$ ($0.0 \leq x \leq 1.0$) nanophotocatalysts: synthesis, characterization and photocatalytic degradation of methylene blue dye. *J. Mol. Struct.* **1119**, 39–47 (2016)
- M.I.A. Abdel Maksoud et al., Insight on water remediation application using magnetic nanomaterials and biosorbents. *Coord. Chem. Rev.* **403**, 213096 (2020)
- O. Alcalá et al., Toroidal cores of $\text{Mn}_x\text{Co}_{1-x}\text{Fe}_2\text{O}_4/\text{PAA}$ nanocomposites with potential applications in antennas. *Mater. Chem. Phys.* **192**, 17–21 (2017)
- M.N. Akhtar et al., Evaluation of structural, morphological and magnetic properties of CuZnNi ($\text{Cu}_x\text{Zn}_{0.5-x}\text{Ni}_{0.5}\text{Fe}_2\text{O}_4$) nanocrystalline ferrites for core, switching and MLCT's applications. *J. Magn. Magn. Mater.* **421**, 260–268 (2017)

17. Ç. Demirci et al., Lanthanum ion substituted cobalt ferrite nanoparticles and their hyperthermia efficiency. *J. Magn. Magn. Mater.* **458**, 253–260 (2018)
18. T. Tatarchuk et al., Structural characterization and antistructure modeling of cobalt-substituted zinc ferrites. *J. Alloys Compd.* **694**, 777–791 (2017)
19. T. Tatarchuk et al., Effect of cobalt substitution on structural, elastic, magnetic and optical properties of zinc ferrite nanoparticles. *J. Alloys Compd.* **731**, 1256–1266 (2018)
20. S. Kane, M. Satalkar, Correlation between magnetic properties and cationic distribution of $Zn_{0.85-x}Ni_xMg_{0.05}Cu_{0.1}Fe_2O_4$ nano spinel ferrite: effect of Ni doping. *J. Mater. Sci.* **52**(6), 3467–3477 (2017)
21. H.K. Fadafan, R.L. Orimi, S. Nezhadeini, Effect of Co doping on the magnetic and DC electrical properties of Mn-Zn nanoferrites. *J. Magn. Magn. Mater.* **456**, 98–103 (2018)
22. A. Hassadee, T. Jutarosaga, W. Onreabroy, Effect of zinc substitution on structural and magnetic properties of cobalt ferrite. *Procedia Eng.* **32**, 597–602 (2012)
23. Y. Köseoğlu et al., Structural and magnetic properties of $Co_xZn_{1-x}Fe_2O_4$ nanocrystals synthesized by microwave method. *Polyhedron* **28**(14), 2887–2892 (2009)
24. R. Sharma et al., Improvement in magnetic behaviour of cobalt doped magnesium zinc nano-ferrites via co-precipitation route. *J. Alloys Compd.* **684**, 569–581 (2016)
25. T.R. Tatarchuk et al., Structural characterization and antistructure modeling of cobalt-substituted zinc ferrites. *J. Alloys Compd.* **694**, 777–791 (2017)
26. N. Moumen, M. Pileni, New syntheses of cobalt ferrite particles in the range 2–5 nm: comparison of the magnetic properties of the nanosized particles in dispersed fluid or in powder form. *Chem. Mater.* **8**(5), 1128–1134 (1996)
27. C. Pham-Huu et al., Microstructural investigation and magnetic properties of $CoFe_2O_4$ nanowires synthesized inside carbon nanotubes. *Phys. Chem. Chem. Phys.* **5**(17), 3716–3723 (2003)
28. H. Deng et al., Monodisperse magnetic single-crystal ferrite microspheres. *Angew. Chem.* **117**(18), 2842–2845 (2005)
29. M. Sajjia et al., Developments of cobalt ferrite nanoparticles prepared by the sol–gel process. *Ceram. Int.* **40**(1), 1147–1154 (2014)
30. D.M. Ghone et al., Microstructure, lattice strain, magnetic and magnetostriction properties of holmium substituted cobalt ferrites obtained by co-precipitation method. *J. Alloys Compd.* (2017). <https://doi.org/10.1016/j.jallcom.2017.12.219>
31. K. Kombaiah et al., Self heating efficiency of $CoFe_2O_4$ nanoparticles: a comparative investigation on the conventional and microwave combustion method. *J. Alloys Compd.* **735**, 1536–1545 (2018)
32. D. Zhang et al., Magnetic-field-induced dielectric behaviors and magneto-electrical coupling of multiferroic compounds containing cobalt ferrite/barium calcium titanate composite fibers. *J. Alloys Compd.* **740**, 1067–1076 (2018)
33. J. Sanchez-Marcos et al., Cation distribution of cobalt ferrite electrosynthesized nanoparticles. A methodological comparison. *J. Alloys Compd.* **739**, 909–917 (2017)
34. S.U. Bhasker et al., Temperature dependent and applied field strength dependent magnetic study of cobalt nickel ferrite nanoparticles: synthesized by an environmentally benign method. *J. Magn. Magn. Mater.* **452**, 398–406 (2018)
35. R. Kumar et al., Tuning of magnetic property by lattice strain in lead substituted cobalt ferrite. *Mater. Sci. Eng. B* **220**, 73–81 (2017)
36. M. Hashim et al., Influence of rare earth ion doping (Ce and Dy) on electrical and magnetic properties of cobalt ferrites. *J. Magn. Magn. Mater.* **449**, 319–327 (2018)
37. R.S. Yadav et al., Structural, magnetic, elastic, dielectric and electrical properties of hot-press sintered $Co_{1-x}Zn_xFe_2O_4$ ($x = 0.0, 0.5$) spinel ferrite nanoparticles. *J. Magn. Magn. Mater.* **447**, 48–57 (2018)
38. K.R. Babu, K.R. Rao, B.R. Babu, Cu^{2+} -modified physical properties of cobalt-nickel ferrite. *J. Magn. Magn. Mater.* **434**, 118–125 (2017)
39. Jauhar, S. and S. Singhal, Substituted cobalt nano-ferrites, $CoM_xFe_{2-x}O_4$ ($M = Cr^{3+}, Ni^{2+}, Cu^{2+}, Zn^{2+}; 0.2 \leq x \leq 1.0$) as heterogeneous catalysts for modified Fenton's reaction. *Ceram. Int.* **40**(8), 11845–11855 (2014)
40. A.H. Ashour et al., Antimicrobial activity of metal-substituted cobalt ferrite nanoparticles synthesized by sol–gel technique. *Particuology* **40**, 141–151 (2018)
41. M.I.A.A. Maksoud et al., Antibacterial, antibiofilm, and photocatalytic activities of metals-substituted spinel cobalt ferrite nanoparticles. *Microb. Pathog.* **127**, 144–158 (2019)
42. M.I.A.A. Maksoud et al., Tunable structures of copper substituted cobalt nanoferrites with prospective electrical and magnetic applications. *J. Mater. Sci.: Mater. Electron.* **30**(5), 4908–4919 (2019)
43. M.I.A. Abdel Maksoud et al., Incorporation of Mn^{2+} into cobalt ferrite via sol–gel method: insights on induced changes in the structural, thermal, dielectric, and magnetic properties. *J. Sol–Gel Sci. Technol.* **90**(3), 631–642 (2019)
44. H.S. Hassan, M.I.A. Abdel Maksoud, L.A. Attia, Assessment of zinc ferrite nanocrystals for removal of ^{134}Cs and $^{152+154}Eu$ radionuclides from nitric acid solution. *J. Mater. Sci.: Mater. Electron.* **31**, 1616–1633 (2019)
45. S. Brunauer, P.H. Emmett, E. Teller, Adsorption of gases in multimolecular layers. *J. Am. Chem. Soc.* **60**(2), 309–319 (1938)
46. C. Wei et al., Synthesis of hierarchically porous $NiCo_2S_4$ core–shell hollow spheres via self-template route for high performance supercapacitors. *Appl. Surf. Sci.* **453**, 288–296 (2018)
47. C. Wei et al., Self-template synthesis of double shelled $ZnS-NiS_{1.97}$ hollow spheres for electrochemical energy storage. *Appl. Surf. Sci.* **435**, 993–1001 (2018)
48. Z. Gao et al., A high surface area superparamagnetic mesoporous spinel ferrite synthesized by a template-free approach and its adsorptive property. *Microporous Mesoporous Mater.* **132**(1), 188–195 (2010)
49. P. Belavi et al., Structural, electrical and magnetic properties of cadmium substituted nickel–copper ferrites. *Mater. Chem. Phys.* **132**(1), 138–144 (2012)
50. K. Ramakrishna et al., Investigation of cation distribution and magnetocrystalline anisotropy of $Ni_xCu_{0.1}Zn_{0.9-x}Fe_2O_4$ nanoferrites: role of constant mole percent of Cu^{2+} dopant in place of Zn^{2+} . *Ceram. Int.* **43**(11), 7984–7991 (2017)
51. M.K. Abbas et al., Impact of Dy on structural, dielectric and magnetic properties of Li-Tb-nanoferrites synthesized by micro-emulsion method. *Ceram. Int.* **43**(7), 5524–5533 (2017)
52. A.V. Humbe et al., Impact of Jahn Teller ion on magnetic and semiconducting behaviour of Ni-Zn spinel ferrite synthesized by nitrate-citrate route. *J. Alloys Compd.* **691**, 343–354 (2017)
53. M. Hashim et al., Preparation and characterization chemistry of nano-crystalline Ni–Cu–Zn ferrite. *J. Alloys Compd.* **549**, 348–357 (2013)
54. V.J. Angadi et al., Effect of $Sm^{3+}-Gd^{3+}$ on structural, electrical and magnetic properties of Mn–Zn ferrites synthesized via combustion route. *J. Alloys Compd.* **656**, 5–12 (2016)
55. A.A. Reheem, M.A. Maksoud, A. Ashour, Surface modification and metallization of polycarbonate using low energy ion beam. *Radiat. Phys. Chem.* **125**, 171–175 (2016)

56. A. Ditta et al., Structural, magnetic and spectral properties of Gd and Dy co-doped dielectrically modified Co-Ni ($\text{Ni}_{0.4}\text{Co}_{0.6}\text{Fe}_2\text{O}_4$) ferrites. *Physica B* **507**, 27–34 (2017)
57. R.H. Kadam et al., Phase evaluation of Li^+ substituted CoFe_2O_4 nanoparticles, their characterizations and magnetic properties. *J. Magn. Magn. Mater.* **355**, 70–75 (2014)
58. O. Josyulu, J. Sobhanadri, The far-infrared spectra of some mixed cobalt zinc and magnesium zinc ferrites. *Phys. Status Solidi (a)* **65**(2), 479–483 (1981)
59. M.K. Raju, FT-IR studies of Cu substituted Ni-Zn ferrites for structural and vibrational investigations. *Chem. Sci. Trans.* **4**(1), 137–142 (2015)
60. M. Amer et al., Characterization and structural and magnetic studies of as-synthesized Fe^{2+} $\text{Cr}_x\text{Fe}_{(2-x)}\text{O}_4$ nanoparticles. *J. Magn. Magn. Mater.* **439**, 373–383 (2017)
61. M. Amer et al., Structural and physical properties of the nanocrystalline Al-substituted Cr-Cu ferrite. *J. Magn. Magn. Mater.* **343**, 286–292 (2013)
62. R. Kadam et al., Phase evaluation of Li^+ substituted CoFe_2O_4 nanoparticles, their characterizations and magnetic properties. *J. Magn. Magn. Mater.* **355**, 70–75 (2014)
63. A. Ghasemi, Compositional dependence of magnetization reversal mechanism, magnetic interaction and Curie temperature of $\text{Co}_{1-x}\text{Sr}_x\text{Fe}_2\text{O}_4$ spinel thin film. *J. Alloys Compd.* **645**, 467–477 (2015)
64. S. Patange et al., Infrared spectral and elastic moduli study of $\text{NiFe}_{2-x}\text{Cr}_x\text{O}_4$ nanocrystalline ferrites. *J. Magn. Magn. Mater.* **325**, 107–111 (2013)
65. M. Amer, Structural and magnetic studies of the $\text{Co}_{1+x}\text{Ti}_x\text{Fe}_{2(1-x)}\text{O}_4$ ferrites. *J. Magn. Magn. Mater.* **426**, 771–778 (2017)
66. M. Amer et al., Structural and magnetic characterization of the $\text{Mg}_{0.2-x}\text{Sr}_x\text{Mn}_{0.8}\text{Fe}_2\text{O}_4$ nanoparticles. *J. Magn. Magn. Mater.* **363**, 60–65 (2014)
67. R.D. Shannon, Revised effective ionic radii and systematic studies of interatomic distances in halides and chalcogenides. *Acta Crystallogr. A* **32**(5), 751–767 (1976)
68. S. Singhal et al., Preparation and characterization of nanosize nickel-substituted cobalt ferrites ($\text{Co}_{1-x}\text{Ni}_x\text{Fe}_2\text{O}_4$). *J. Solid State Chem.* **178**(10), 3183–3189 (2005)
69. P. Guo et al., Electrochemical properties of colloidal nanocrystal assemblies of manganese ferrite as the electrode materials for supercapacitors. *J. Mater. Sci.* **52**(9), 5359–5365 (2017)
70. S. Yadav et al., Distribution of cations in $\text{Co}_{1-x}\text{Mn}_x\text{Fe}_2\text{O}_4$ using XRD, magnetization and Mössbauer spectroscopy. *J. Alloys Compd.* **646**, 550–556 (2015)
71. K.V. Babu et al., Effects of copper substitution on the microstructural, electrical and magnetic properties of $\text{Ni}_{0.7}\text{Co}_{0.3-x}\text{Cu}_x\text{Fe}_2\text{O}_4$ ferrites. *J. Phys. Chem. Solids* **118**, 172–185 (2018)
72. L. Kumar, P. Kumar, M. Kar, Cation distribution by Rietveld technique and magnetocrystalline anisotropy of Zn substituted nanocrystalline cobalt ferrite. *J. Alloys Compd.* **551**, 72–81 (2013)
73. D. Jnaneshwara et al., Role of Cu^{2+} ions substitution in magnetic and conductivity behavior of nano- CoFe_2O_4 . *Spectrochim. Acta A* **132**, 256–262 (2014)
74. J. Balavijayalakshmi, N. Suriyanarayanan, R. Jayaprakash, Influence of copper on the magnetic properties of cobalt ferrite nanoparticles. *Mater. Lett.* **81**, 52–54 (2012)
75. M. Gabal, Y. Al Angari, M. Kadi, Structural and magnetic properties of nanocrystalline $\text{Ni}_{1-x}\text{Cu}_x\text{Fe}_2\text{O}_4$ prepared through oxalates precursors. *Polyhedron* **30**(6), 1185–1190 (2011)
76. M. Amer et al., Structural properties and magnetic interactions in Sr-doped Mg–Mn nanoparticle ferrites. *Mater. Chem. Phys.* **162**, 442–451 (2015)
77. G. Mustafa et al., Investigation of structural and magnetic properties of Ce^{3+} -substituted nanosized Co–Cr ferrites for a variety of applications. *J. Alloys Compd.* **618**, 428–436 (2015)
78. K.H. Maria, S. Choudhury, M.A. Hakim, Structural phase transformation and hysteresis behavior of Cu-Zn ferrites. *Int. Nano Lett.* **3**(1), 42 (2013)
79. N. Sanpo et al., Biocompatibility of transition metal-substituted cobalt ferrite nanoparticles. *J. Nanopart. Res.* **16**(7), 2510 (2014)
80. R.S. Yadav et al., Impact of grain size and structural changes on magnetic, dielectric, electrical, impedance and modulus spectroscopic characteristics of CoFe_2O_4 nanoparticles synthesized by honey mediated sol–gel combustion method. *Adv. Nat. Sci.: Nanosci. Nanotechnol.* **8**(4), 045002 (2017)
81. N. Sanpo, C.C. Berndt, J. Wang, Microstructural and antibacterial properties of zinc-substituted cobalt ferrite nanopowders synthesized by sol–gel methods. *J. Appl. Phys.* **112**(8), 084333 (2012)
82. E.R. Kumar et al., Structural, dielectric and gas sensing behavior of Mn substituted spinel MFe_2O_4 ($\text{M} = \text{Zn}, \text{Cu}, \text{Ni}$, and Co) ferrite nanoparticles. *J. Magn. Magn. Mater.* **398**, 281–288 (2016)
83. M.T. Rahman, M. Vargas, C. Ramana, Structural characteristics, electrical conduction and dielectric properties of gadolinium substituted cobalt ferrite. *J. Alloys Compd.* **617**, 547–562 (2014)
84. M.A. Maksoud et al., La^{3+} doped $\text{LiCo}_{0.25}\text{Zn}_{0.25}\text{Fe}_2\text{O}_4$ spinel ferrite nanocrystals: insights on structural, optical, and magnetic properties. *J. Rare Earths.* (2020). <https://doi.org/10.1016/j.jre.2019.12.017>
85. K.M. Srinivasamurthy et al., Tuning of ferrimagnetic nature and hyperfine interaction of Ni^{2+} doped cobalt ferrite nanoparticles for power transformer applications. *Ceram. Int.* **44**(8), 9194–9203 (2018)
86. M.A. Maksoud et al., Influence of Mg^{2+} substitution on structural, optical, magnetic, and antimicrobial properties of Mn–Zn ferrite nanoparticles. *J. Mater. Sci.: Mater. Electron.* **31**(3), 2598–2616 (2020)
87. H. Abdallah, T. Moyo, J. Msomi, The effect of annealing temperature on the magnetic properties of $\text{Mn}_x\text{Co}_{1-x}\text{Fe}_2\text{O}_4$ ferrites nanoparticles. *J. Supercond. Novel Magn.* **25**(8), 2625–2630 (2012)
88. I. Sharifi, H. Shokrollahi, Structural, magnetic and Mössbauer evaluation of Mn substituted Co–Zn ferrite nanoparticles synthesized by co-precipitation. *J. Magn. Magn. Mater.* **334**, 36–40 (2013)
89. C. Ren, Z. Zhang, R. Yang, The construction of three-dimensionally ordered macroporous ($\text{Fe}, \text{Zn}, \text{Cu}, \text{Co}$)/ LaMnO_3 with controllable gelation rate and their catalytic combustion properties. *J. Porous Mater.* **26**(6), 1649–1656 (2019)
90. M. Abdel Maksoud et al., Unveiling the effect of Zn^{2+} substitution in enrichment of structural, magnetic, and dielectric properties of cobalt ferrite. *J. Inorg. Organomet. Polym. Mater.* (2020). <https://doi.org/10.1007/s10904-020-01523-8>
91. M.A. Elkodous et al., Fabrication of ultra-pure anisotropic zinc oxide nanoparticles via simple and cost-effective route: implications for UTI and EAC medications. *Biol. Trace Elem. Res.* (2019). <https://doi.org/10.1007/s12011-019-01894-1>
92. I. Gul et al., Structural, magnetic and electrical properties of $\text{Co}_{1-x}\text{Zn}_x\text{Fe}_2\text{O}_4$ synthesized by co-precipitation method. *J. Magn. Magn. Mater.* **311**(2), 494–499 (2007)
93. W. Wooster, Physical properties and atomic arrangements in crystals. *Rep. Prog. Phys.* **16**(1), 62 (1953)
94. K. Modi et al., Study of infrared spectroscopy and elastic properties of fine and coarse grained nickel–cadmium ferrites. *J. Mater. Sci.* **41**(22), 7308–7318 (2006)

95. V. Patil et al., Effect of zinc substitution on structural and elastic properties of cobalt ferrite. *J. Alloys Compd.* **488**(1), 199–203 (2009)
96. E. El-Ghazzawy, M. Amer, Structural, elastic and magnetic studies of the as-synthesized $\text{Co}_{1-x}\text{Sr}_x\text{Fe}_2\text{O}_4$ nanoparticles. *J. Alloys Compd.* **690**, 293–303 (2017)
97. S. Patange et al., Elastic properties of nanocrystalline aluminum substituted nickel ferrites prepared by co-precipitation method. *J. Mol. Struct.* **1038**, 40–44 (2013)
98. R.A. Pawar et al., Spectroscopic, elastic and dielectric properties of Ho^{3+} substituted Co-Zn ferrites synthesized by sol-gel method. *Ceram. Int.* **42**(14), 16096–16102 (2016)
99. A. Bhaskar, S. Murthy, Effect of sintering temperatures on the elastic properties of Mn (1%) added MgCuZn ferrites. *J. Magn. Magn. Mater.* **355**, 100–103 (2014)
100. S. Algude et al., Elastic behaviour of Cr^{3+} substituted Co-Zn ferrites. *J. Magn. Magn. Mater.* **350**, 39–41 (2014)
101. S.E. Shirsath et al., Structure refinement, cation site location, spectral and elastic properties of Zn^{2+} substituted NiFe_2O_4 . *J. Mol. Struct.* **1024**, 77–83 (2012)
102. R. Pawar et al., Inter-atomic bonding and dielectric polarization in Gd^{3+} incorporated Co-Zn ferrite nanoparticles. *Physica B* **510**, 74–79 (2017)
103. S. Jauhar, S. Singhal, Substituted cobalt nano-ferrites, $\text{CoM}_x\text{Fe}_{2-x}\text{O}_4$ ($\text{M} = \text{Cr}^{3+}, \text{Ni}^{2+}, \text{Cu}^{2+}, \text{Zn}^{2+}; 0.2 \leq x \leq 1.0$) as heterogeneous catalysts for modified Fenton's reaction. *Ceram. Int.* **40**(8), 11845–11855 (2014)
104. M. Atif et al., Effect of Mn substitution on the cation distribution and temperature dependence of magnetic anisotropy constant in $\text{Co}_{1-x}\text{Mn}_x\text{Fe}_2\text{O}_4$ ($0.0 \leq x \leq 0.4$) ferrites. *Ceram. Int.* **40**(1), 471–478 (2014)
105. I. Sharifi, H. Shokrollahi, Nanostructural, magnetic and Mössbauer studies of nanosized $\text{Co}_{1-x}\text{Zn}_x\text{Fe}_2\text{O}_4$ synthesized by co-precipitation. *J. Magn. Magn. Mater.* **324**(15), 2397–2403 (2012)
106. M. Atif et al., Synthesis and investigation of structural, magnetic and dielectric properties of zinc substituted cobalt ferrites. *J. Phys. Chem. Solids* **123**, 36–42 (2018)
107. B.C. Sekhar et al., Magnetic and magnetostrictive properties of Cu substituted Co-ferrites. *J. Magn. Magn. Mater.* **398**, 59–63 (2016)
108. H. El Moussaoui et al., Experimental studies of neodymium ferrites doped with three different transition metals. *Mater. Lett.* **171**, 142–145 (2016)
109. X. Guoxi, X. Yuebin, Effects on magnetic properties of different metal ions substitution cobalt ferrites synthesis by sol-gel auto-combustion route using used batteries. *Mater. Lett.* **164**, 444–448 (2016)
110. T.W. Mammo et al., Studies of structural, morphological, electrical, and magnetic properties of Mg-substituted Co-ferrite materials synthesized using sol-gel autocombustion method. *Physica B* **523**, 24–30 (2017)
111. A. Ashour et al., Antimicrobial activity of metal-substituted cobalt ferrite nanoparticles synthesized by sol-gel technique. *Particuology*, **40**, 141–151 (2018)
112. M.A. Maksoud et al., Synthesis and characterization of metals-substituted cobalt ferrite $[\text{Co}_{(1-x)}\text{M}_x]\text{Fe}_2\text{O}_4$; ($\text{M} = \text{Zn}, \text{Cu}, \text{Mn}; x = 0, 0.5$) nanoparticles as antimicrobial agents and sensors for Anagrelide determination in biological samples. *Mater. Sci. Eng.* **92**, 644–656 (2018)
113. S. Bhukal, S. Singhal, Magnetically separable copper substituted cobalt-zinc nano-ferrite photocatalyst with enhanced photocatalytic activity. *Mater. Sci. Semicond. Process.* **26**, 467–476 (2014)

Publisher's Note Springer Nature remains neutral with regard to jurisdictional claims in published maps and institutional affiliations.